ACS NANO

www.acsnano.org

ARTICLE

Demonstration of Two-Dimensional Exciton Complex Palette

Sanghyeok Park,[‖] Jaeyu Kim,[‖] Dongha Kim, Kenji Watanabe, Takashi Taniguchi, and Min-Kyo Seo*

Cite This: *ACS Nano* 2024, 18, 5647−5655

Read Online

ACCESS | Metrics & More | Article Recommendations | Supporting Information

ABSTRACT: **Exciton complexes in two-dimensional semiconductors, encompassing bright and dark excitons, biexcitons, and defect-bound excitons, have shown significant potential across a wide range of research areas. These applications range from exploring quantum many-body phenomena to developing nonclassical light sources and quantum transport devices. To fully leverage their dynamic and interactive properties and extend the capabilities of excitonic devices, realizing systematic engineering and mixing of the exciton complexes are crucial. Unlike conventional material methods, which often lead to undesired changes in the electronic band structure and binding energy, optical methods provide a means to manipulate the radiative decay dynamics of individual exciton complexes in a purely environmental manner. Here, we employ a specialized photonic platform, analogous to an artist's palette, to arrange and mix exciton complexes on an identical two-dimensional transition metal dichalcogenide medium. Essentially, a gradient thickness mirror (GTM) continuously tunes the local distribution of optical vacuum field interference. The GTM platform enables us to create and examine five distinct compositions of the exciton complexes of the WSe_2 monolayer and their contributions to the photoluminescence spectrum. Moreover, the exciton complex palette facilitates the observation of dark and defect-bound excitons, even at high temperatures of 70 K, and its performance can be further managed by simple postprocessing manipulations.**

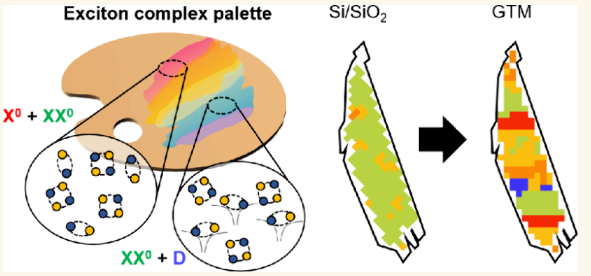

KEYWORDS: *exciton complexes, transition metal dichalcogenide, radiative decay dynamics, gradient thickness mirror, vacuum-field interference*

Two-dimensional (2D) exciton complexes found in monolayer transition metal dichalcogenides (TMDCs), encompassing bright and dark excitons, biexcitons, and defect-bound excitons, exhibit distinct properties that are useful across various research domains, ranging from quantum optics to many-body physics.[1,2] Bright neutral excitons, characterized by their high quantum efficiency, endow TMDC media with strong potential for the development of ultrathin, high-performance optoelectronic devices.[3−8] Biexcitons, with their intrinsic two-photon interaction properties, can demonstrate entangled photon pair sources.[9−11] Additionally, their high valley selectivity exhibits the possibility of high-visibility valleytronic devices.[12] Dark excitons, owing to the spin-forbidden recombination, exhibit long lifetimes, a fundamental attribute that is essential the observation of quantum many-body phenomena, such as Bose−Einstein condensation, and long-distance exciton transport.[13−17] The diffusion of charged excitons (also called trions) can be easily controlled by a simple electrical bias. They offer significant advantages in excitonic transport devices over other exciton complexes.[18] In addition, defect-bound excitons have attracted attention due to the local-state-induced reduction of exciton−exciton collisions and the absence of intervalley scattering, thereby extending exciton lifetime and valley-polarization lifetime.[19,20]

TMDC exciton complexes exist in the form of a mixture and exhibit various interplays.[9,21−26] To explore the roles and potential of individual exciton complexes, it is necessary to systematically create and control their ensemble compositions. An in-depth investigation is required for exploring the effects of the interactions and competition among the exciton complexes for optoelectronic device applications and the realization of quantum many-body phenomena. Moreover, the refinement of a desired exciton complex can enhance the performance of excitonic devices: nonclassical light sources with higher fidelity, exciton transport devices with longer diffusion lengths, and valleytronic devices with increased

Received: November 12, 2023
Revised: February 5, 2024
Accepted: February 7, 2024
Published: February 9, 2024

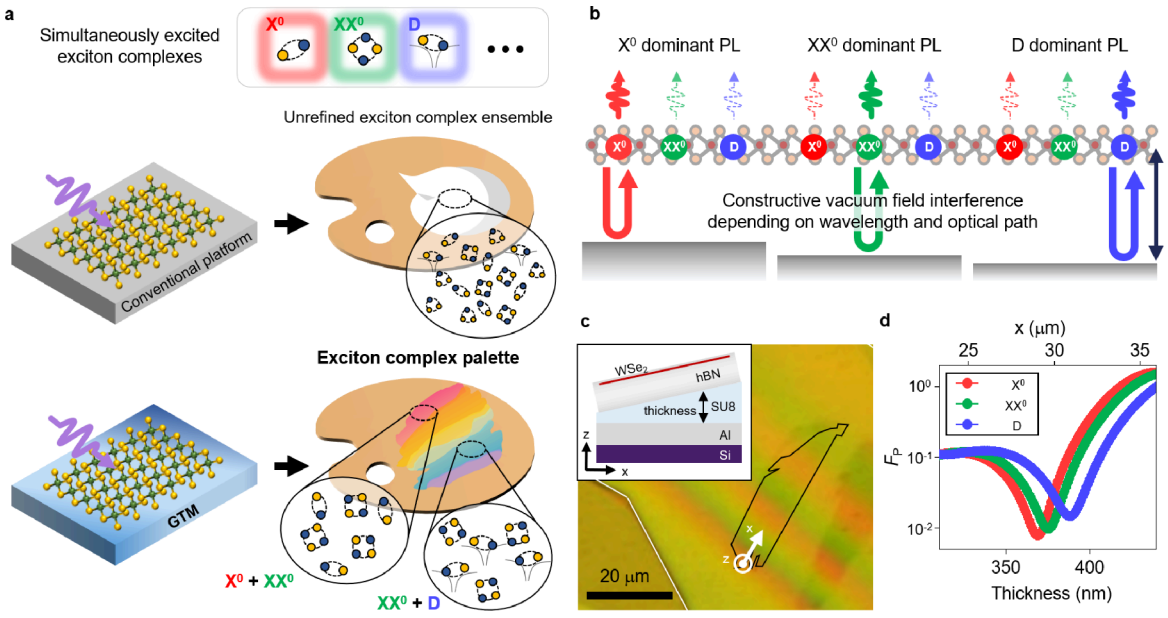

Figure 1. Gradient thickness mirror platform demonstrating the exciton complex palette. (a) Schematic of the exciton complex palette for on-demand tuning of the ensemble composition of exciton complexes in a single WSe_2 monolayer. (b) Schematic of the radiative decay control of exciton complexes. Constructive (destructive) vacuum field interference by the mirror enhances (suppresses) the radiative decay rate of a specific exciton complex over the others. (c) Optical microscope image of the fabricated GTM and the hBN-encapsulated WSe_2 monolayer (the black solid polygon). The white arrow indicates the coordinate origin and the *x*-axis (the long axis of the monolayer WSe_2 flake), which is approximately parallel to the thickness gradient of the SU8 layer. Schematic cross-section of the entire sample structure is presented in the inset of (c). (d) Calculated Purcell factor at the emission wavelengths of the bright neutral exciton (X^0), biexciton (XX^0), and defect-bound exciton (D) as a function of the thickness of the SU8 layer. The upper axis of the plot represents the position (*x*) from the origin along the white arrow in (c).

visibility. However, the primary material methodologies, such as strain, defect implantation, and electrostatic bias, introduce undesired changes in the electronic band structure and exciton binding energy,[3,27−31] leading to the loss or uncontrolled change of key properties of the exciton complexes. Additionally, the significant variances in specimens have to be considered.

Optical methods employing plasmonic nanostructures, photonic crystals, metasurfaces, or even simple planar mirrors[4,32−38] provide a means to manipulate radiative decay dynamics of bright neutral excitons in a purely environmental manner. The present juncture calls for the optical manipulation of the decay dynamics of not only the neutral exciton but also other exciton complexes, challenging their closely spaced emission wavelengths (on the order of a few nm). Particularly, we aim to demonstrate a specialized photonic platform that can create various ensemble compositions of the exciton complexes and diversify their contributions to the optical response of the employed TMDC material. We present an exciton complex palette to arrange and mix the exciton complexes on the space of a flat and identical TMDC medium (Figure 1a), analogous to an artist's palette. Employing a simple gradient thickness mirror (GTM), we can continuously tune the local distribution of the optical vacuum field at the plane of the TMDC material by varying the distance from the reflecting layer (Figure 1b). The constructive (destructive) interference for the emission wavelength of a specific exciton complex enhances its radiative decay rate (lifetime) compared to the other exciton complexes. We successfully achieved the systematic and continuous creation of five distinct compositions of the exciton complexes on a single TMDC material, allowing for the self-consistent analysis of their photoluminescence (PL) behaviors. The exciton complex palette operated even at a high temperature of 70 K, making it a convenient and cost-effective experimental methodology.

RESULTS AND DISCUSSION

Gradient Thickness Mirror Platform. The GTM comprised a sloped SU8 layer deposited on a Si substrate, topped by an 80 nm thick Al layer that acted as a bottom mirror (inset of Figure 1c). The tungsten diselenide (WSe_2) monolayer encapsulated by hexagonal boron nitride (hBN) was dry-transferred to the SU8 layer. The thicknesses of the bottom and top hBN layers were 230 and 10 nm, respectively. The distance of the WSe_2 monolayer from the Al mirror is large enough to neglect the effects of surface plasmon polaritons on the metallic Al mirror (Supporting Information, Section S1). The spin-coating successfully created the sloped SU8 layer with a uniform thickness gradient of ~1° over a large area of tens of micrometers. After thermal annealing, the SU8 layer became chemically and mechanically robust enough to withstand the transfer process of the 2D materials. In Figure 1c, the optical microscopy image of the GTM clearly displays the white light interference pattern across the thickness gradient of the SU8 layer. The color change in the white light interference reflects the change in the constructive interference wavelength. Over the region of a 35 μm long WSe_2 monolayer (the solid black contour in Figure 1c), the thickness of the SU8 layer varies from 80 to 440 nm (Supporting Information, Section S2). Given the small gradient slope, the optical behavior of the demonstrated GTM can be described by thin-film theory.

In Figure 1d, we calculated the Purcell factor at the position of the WSe_2 monolayer as a function of the SU8 layer thickness

https://doi.org/10.1021/acsnano.3c11214
ACS Nano 2024, 18, 5647−5655

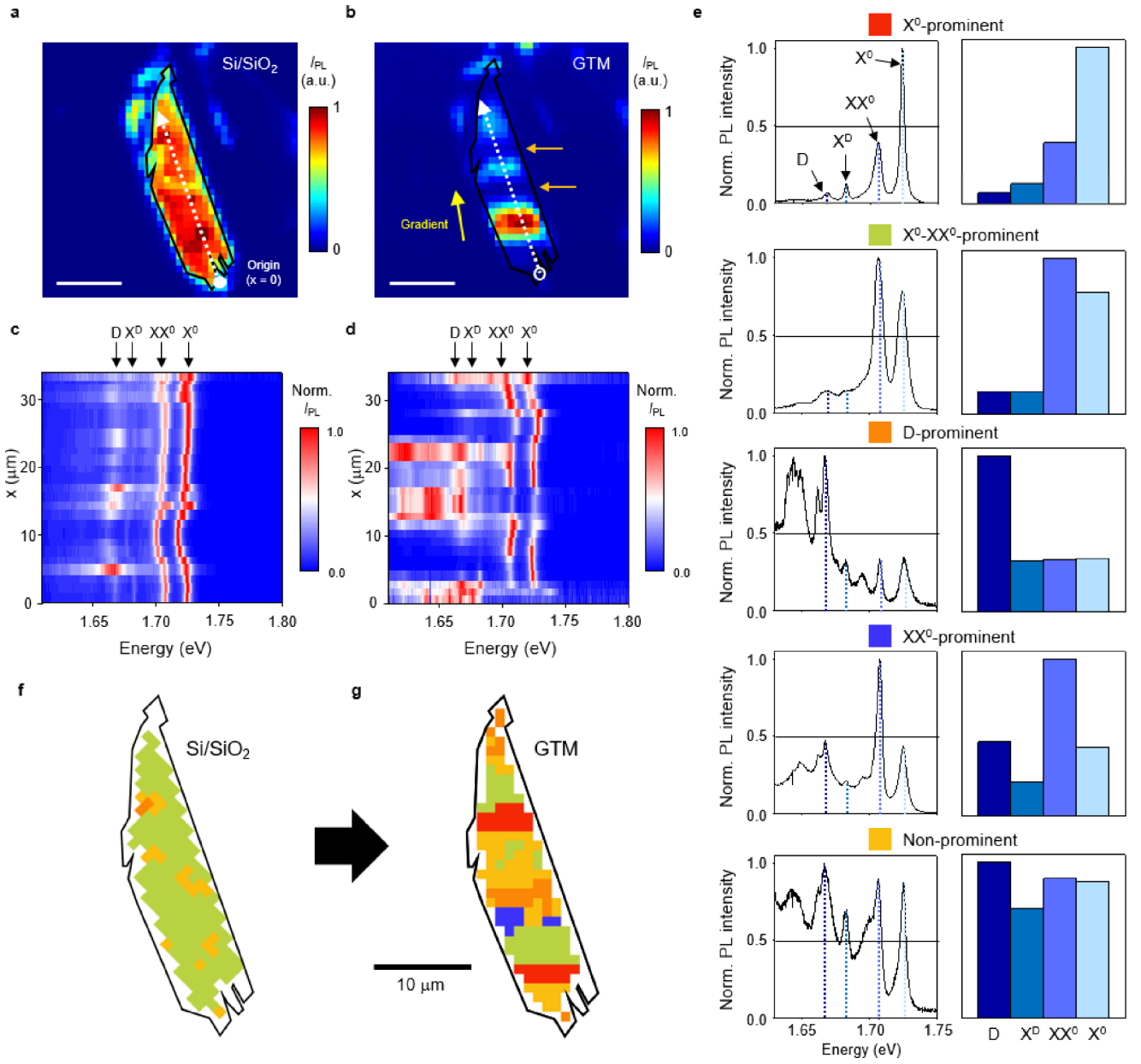

Figure 2. Demonstration of the exciton complex palette. (a, b) Measured total PL intensity distribution from the hBN-encapsulated WSe_2 monolayer (the black solid polygon) on the flat Si/SiO_2 substrate (a) and on the GTM (b). The PL intensity is integrated over the photon energy range from 1.65 to 1.75 eV. Scale bar, 10 μm. The yellow arrow indicates the direction of the thickness gradient, while the orange arrows in (b) highlight the local minima of the PL intensity. (c, d) The position-dependent normalized PL spectra across the center of the monolayer on the flat Si/SiO_2 substrate (c) and on the GTM (d). The left axis of the plot indicates the position (x) from the origin, following the white dashed arrow in (a) and (b). (e) The five representative normalized PL spectra (left panel) contributed by the bright neutral exciton (X^0), biexciton (XX^0), dark exciton (X^D), and defect-bound exciton (D) and their relative peak intensity bar graphs (right panel). (f, g) Spatial distribution of the five different groups on the Si/SiO_2 substrate (f) and on the GTM (g) over the area of the WSe_2 monolayer. The red, green, orange, blue, and yellow colors indicate the X^0-prominent, X^0-XX^0-prominent, XX^0-prominent, D-prominent, and nonprominent cases, respectively. Scale bar, 10 μm.

in the GTM. This calculation was based on the coherent optical feedback model (Supporting Information, Section S3).[34,36] The Purcell effect either suppresses or enhances the emission of an exciton complex under destructive or constructive interference of the vacuum field. In the GTM, the spatial positions and periods of the constructive and destructive interference vary, depending on the wavelength of light. The bright neutral exciton (X^0), biexciton (XX^0), and defect-bound exciton (D) in the employed WSe_2 monolayer emit photons with the wavelengths of 722 nm ($\hbar\omega$ = 1.72 eV), 729 nm (1.70 eV), and 744 nm (1.67 eV), respectively. By relatively modulating the radiative decay rates of bright neutral excitons, biexcitons, and defect-bound excitons along the thickness gradient, the GTM produces various combinations of exciton complexes on a single platform, that is, a palette of exciton complexes. Our GTM platform consistently supports the condition of high-degree destructive interference at any wavelength, owing to the high reflectance of the Al bottom mirror (>0.89 over the wavelength range of the exciton complex PL from 720 to 760 nm) and the continuous

https://doi.org/10.1021/acsnano.3c11214
ACS Nano 2024, 18, 5647−5655

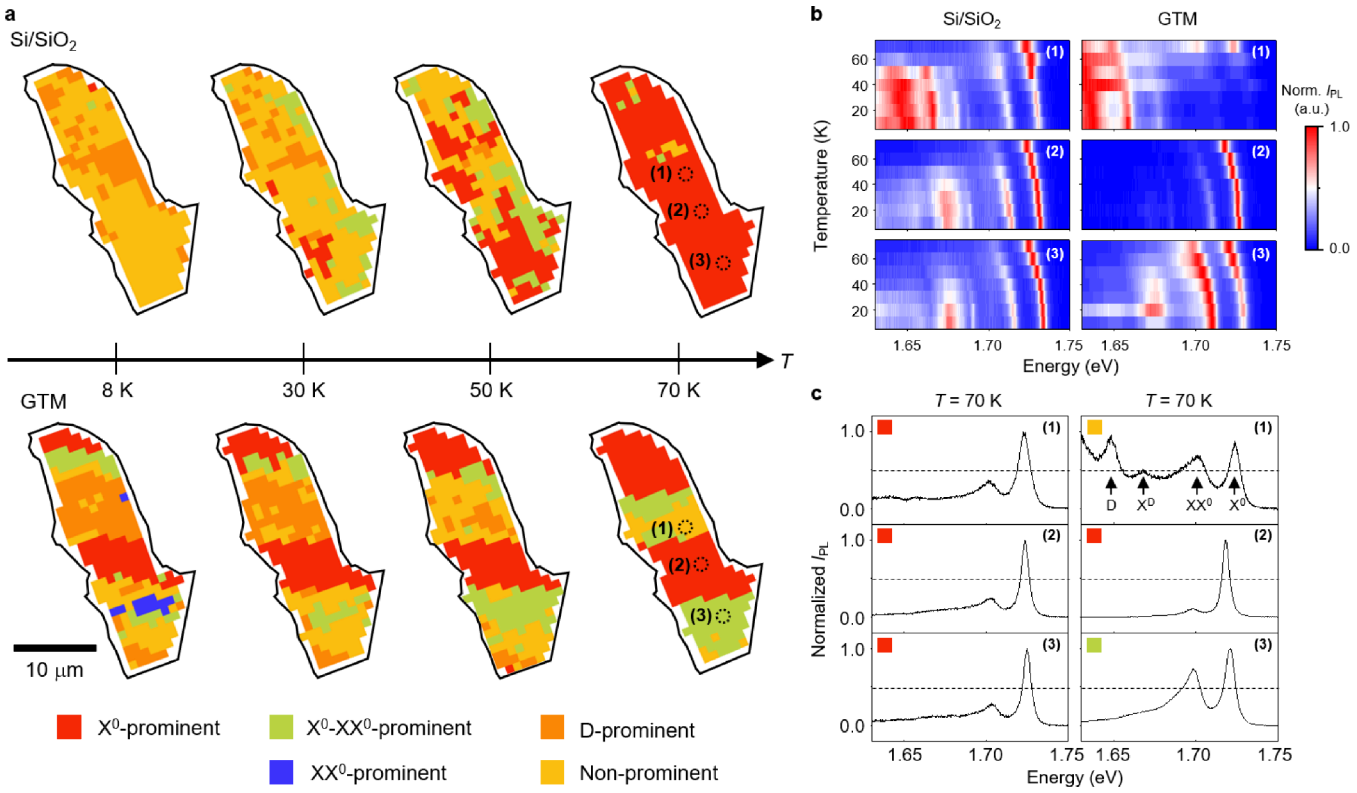

Figure 3. Temperature-dependent behavior of the exciton complex palette. (a) Spatial distribution of the ensemble compositions of the exciton complexes at the temperatures from 8 to 70 K over the area of the WSe_2 monolayer on the Si/SiO_2 substrate (upper panel) and on the GTM (lower panel). The colors indicate the five compositions as shown in Figure 2. Scale bar, 10 μm. (b) The normalized PL spectra based on the temperature from the three different positions indicated in (a). The left and right panels show the PL spectra of the WSe_2 monolayer on the Si/SiO_2 substrate and on the GTM, respectively. The temperature ranges from 8 to 70 K in increments of 10 K, covering values of 8, 20, 30, 40, 50, 60, and 70 K. (c) Normalized PL spectra for each position at 70 K on the Si/SiO_2 substrate (left panel) and on the GTM (right panel).

thickness variation of the SU8 layer. Note that the significant suppression of the radiative decay rate of a particular exciton element allows for the generation of PL spectra featuring a high-contrast combination of exciton complexes. With a sufficiently low optical thickness slope, the GTM effectively discriminates the positions where the emissions of bright neutral excitons, biexcitons, and defect-bound excitons are minimized (or maximized), despite their closely spaced emission wavelengths. We note that, for the same physical thickness gradient slope, replacing the SU8 layer with a dielectric layer of lower refractive index improves the spatial discrimination of different ensemble compositions of the exciton complexes. In the GTM, as calculated in Figure 1d, the positions where the radiative decay of biexcitons and defect-bound excitons is minimized are 0.58 and 1.85 μm away from that of bright neutral excitons, respectively. These values are not only large enough to be resolved by optical microscopy, but are also comparable to the typical exciton diffusion lengths.[39−41]

Demonstration of an Exciton Complex Palette. We experimentally demonstrated the GTM-based exciton complex palette and analyzed its properties via PL intensity and spectrum measurements using a confocal optical microscope and a cryostat (Methods). A 633 nm wavelength laser with a power of 0.25 mW was employed to excite the PL of the WSe_2 monolayer exciton complexes at a temperature of 8 K. As shown in Figure 2a, the hBN-encapsulated WSe_2 monolayer on a flat Si/SiO_2 substrate exhibits a spatially uniform total PL intensity distribution over its area. The normalized standard deviation of the total PL intensity ($\sigma(I)/I_{mean}$) is only ~0.15, indicating spatial uniformity of the prepared WSe_2 monolayer. However, after transfer onto the GTM platform, the WSe_2 monolayer shows a spatially modulated total PL intensity with a distinct stripe pattern (Figure 2b). By manipulating not only the Purcell effect of the emission but also the concentration of the pump light in the WSe_2 monolayer, the GTM can vary the total PL intensity by 2 orders of magnitude (~95.5). The coherent optical feedback model can successfully predict the position-dependent total PL intensity (Supporting Information, Section S4). The first and second PL intensity minima (indicated by the orange arrows in Figure 2b) occur at x = 16.5 and 24.8 μm from the origin, respectively. The calculated positions are x = 17.1 and 29.0 μm, which agree well with the experimental results, considering the spatial resolution of the confocal optical microscope (~1.33 μm) and the small quadratic or higher order variations in the thickness of the spin-coated SU8 layer. While the first minimum results from the minimized pump intensity, the second minimum originates from the suppressed radiative decay of the bright neutral excitons.

Analysis of the PL spectra reveals how the GTM tunes the radiative decay dynamics of the exciton complexes. Figure 2c and d depict the PL spectra measured along a line (the white dotted line in Figure 2a,b) through the center of the WSe_2 monolayer on the flat Si/SiO_2 substrate and the GTM, respectively. Here, we plotted the normalized PL spectra to

https://doi.org/10.1021/acsnano.3c11214
ACS Nano 2024, 18, 5647−5655

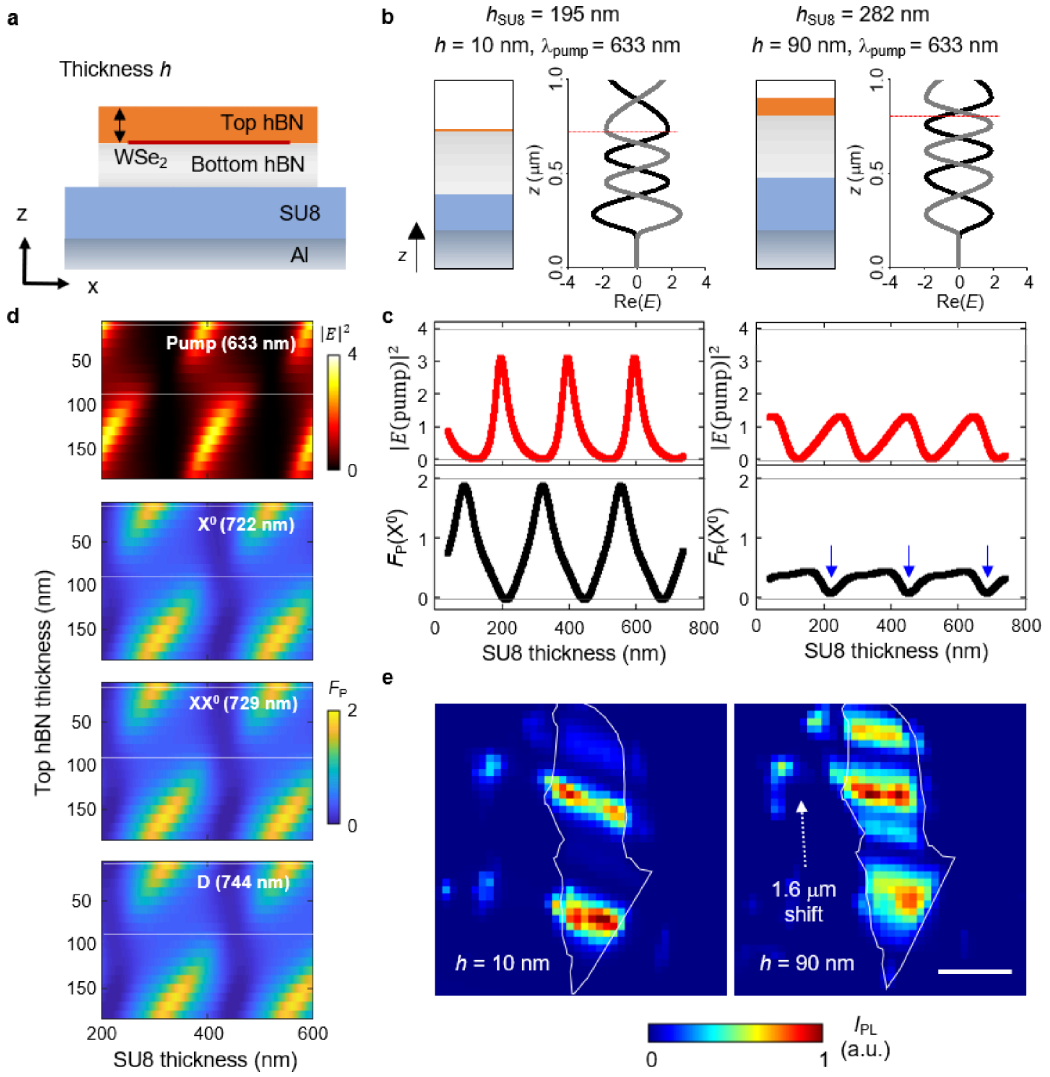

Figure 4. Postprocessing adjustability of the GTM performance. (a) Schematic cross-section of the GTM in relation to the thickness (h) of the top hBN layer. (b) Calculated electric field distribution at the pump wavelength in the Al/SU8/bottom hBN (330 nm)/top hBN multilayer. The red dashed line indicates the position of the WSe_2 monolayer. (c) Calculated pump electric field intensity and Purcell factor for bright neutral excitons at the position of the WSe_2 monolayer depending on the SU8 layer thickness. (d) Calculated pump electric field intensity (λ_{pump} = 633 nm) and Purcell factor for bright neutral exciton (λ_{X0} = 722 nm), biexciton (λ_{XX0} = 729 nm), and defect-bound exciton (λ_D = 744 nm) as a function of the thicknesses of the SU8 layer and the top hBN layer. (e) Normalized total PL intensity distribution measured before and after postprocessing with an additional top hBN layer. The sample is identical to the one shown in Figure 3, which is initially covered by the 10 nm thick top hBN layer. The thickness of the additional hBN layer is 80 nm, resulting in a final top hBN layer thickness of 90 nm. The white solid line outlines the WSe_2 monolayer. The postprocessing adjustment also includes a physical shift of ~1.60 μm along a specific direction indicated by the white dotted arrow. The temperature was 8 K. Scale bar, 10 μm.

facilitate comparisons of the relative emission intensities and ratios among the exciton complexes. The unnormalized PL spectra are presented in Supporting Information, Section S5. On the flat Si/SiO_2 substrate, we observed typical PL spectra dominated by bright neutral excitons (X^0) and biexcitons (XX^0), the profiles for which remain consistent regardless of the position. The PL emissions from dark excitons (X^D) and defect-bound excitons (D) were also well resolved. The ratios of the peak PL intensity of biexcitons, dark excitons, and defect-bound excitons to that of bright neutral excitons were 0.72 ± 0.077, 0.24 ± 0.063, and 0.37 ± 0.18, respectively. Conversely, in the GTM, we observed dramatic and diverse changes in the relative intensity ratios and the dominant element(s) of the exciton complexes in the PL spectrum. The ratio of the peak PL intensity of biexcitons to that of bright neutral excitons varied from 0.26 to 1.97 depending on the position. The PL emissions from other exciton complex elements also undergo dramatic relative intensity changes. These significant changes in the relative PL intensity ratios of the exciton complexes are a result of engineering their radiative decay rates by the GTM. In addition, the experimentally obtained PL intensities of the bright neutral exciton and biexciton and their ratio align well with the theoretical results (Supporting Information, Section S4).

The GTM acted as a versatile palette of exciton complexes, blending the contributions of bright neutral excitons, biexcitons, dark excitons, and defect-bound excitons in various relative proportions. These mixed combinations were then arranged along the direction of the thickness gradient. By providing a single TMDC material with various optical

https://doi.org/10.1021/acsnano.3c11214
ACS Nano 2024, 18, 5647−5655

circumstances, the GTM allows for refined experiments with high consistency in the properties of the exciton complexes. We classified the mixed combinations based on the relative peak PL intensities of the exciton complexes. Setting the criterion of half the peak PL intensity of the most dominant element for categorization, we identified five distinct groups: bright-neutral-exciton-prominent, exciton-biexciton-prominent, biexciton-prominent, defect-bound-exciton-prominent, and nonprominent. Figure 2e shows the representative PL spectra of the five groups and bar graphs of the peak PL intensities of each exciton complex element. On the flat Si/SiO_2 substrate, the X^0-XX^0-prominent group dominantly appeared with 87% of the total area and no diversity was found (Figure 2f). However, on the GTM platform, in addition to the X^0-XX^0-prominent group (29% of the total area), all the X^0-prominent (17%), XX^0-prominent (6%), the D-prominent (14%), and nonprominent (34%) groups emerged (Figure 2g).

High-Temperature Operation of Exciton Complex Palette. One of the notable capabilities of the GTM platform is the formation of diverse combinations of exciton complexes, even at comparatively high temperatures. We fabricated another sample with a 330 (10) nm thick bottom (top) hBN layer and measured the PL spectra at different temperatures ranging from 8 to 70 K, both on the flat Si/SiO_2 substrate and on the GTM platform (Figure 3). Typically, with increasing temperature, the emissions of exciton complexes other than bright neutral excitons become significantly weaker due to their lower binding energies.[42] Consequently, at the temperature of 70 K, the WSe_2 monolayer on the flat Si/SiO_2 substrate primarily exhibits X^0-prominent PL emission, covering ∼96% of its area (top panel of Figure 3a). As the temperature reduces, PL emissions from biexcitons and defect-bound excitons sporadically emerge throughout the WSe_2 monolayer, and at 8 K, nonprominent PL emission occupies ∼74% of the entire area. However, the GTM provides the WSe_2 monolayer with a robust and systematic opportunity to have PL emissions from the exciton complexes that are rarely observed at a certain temperature (bottom panel of Figure 3a). At 8 K, the GTM supports the regions of all five groups, which is an excellent reproduction of the result in Figure 2. Even at 70 K, the GTM allows for the regions of the X^0-XX^0-prominent (32% of the total area) and nonprominent (13%) groups in addition to that of the X^0-prominent group (55%). In fact, the optical control facilitated by the GTM effectively overrides the thermal changes.

We selected three different positions (black dotted circles in Figure 3a) and examined the normalized PL spectra in relation to the temperature, as shown in Figure 3b. On the Si/SiO_2 substrate, as the temperature increases, the PL emission peaks of all exciton complexes show typical red-shifts, with the bright neutral exciton peak becoming dominant regardless of the position. Conversely, on the GTM, the position-dependent, effective engineering of the radiative decay dynamics results in significant diversity in the PL spectra. At position (1), the emissions from the exciton complexes other than the bright neutral exciton remain substantial, or even dominate over all temperatures. By contrast, at positions (2) and (3), the bright neutral exciton and the biexciton emission play a significant role in characterizing the PL spectra, respectively. Figure 3c shows the PL spectra measured at the selected positions at 70 K. For the Si/SiO_2 substrate, the PL spectra are almost identical, showing a dominant bright neutral exciton peak and a secondary biexciton peak. However, the GTM allows us to observe the PL emissions of the exciton complex elements, which are typically active at cryogenic temperatures requiring liquid helium, even at the high temperature of 70 K: dark excitons and defect-bound excitons at position (1) and biexcitons at position (3). Moreover, at position (2), the GTM produces a higher purity emission of bright neutral excitons compared to that of the Si/SiO_2 substrate. The GTM showcases the potential of manipulating radiative decay dynamics through photonic platforms to examine and utilize excitonic fine structures of 2D materials at high temperatures.

Postprocessing of the GTM Performance. Manipulating the thickness of the top hBN layer covering the WSe_2 monolayer provides an additional degree of freedom to tune the behavior and performance of the GTM during postprocessing (Figure 4a). In Figure 4b, we calculate the electric field distribution at the pump wavelength employing the transfer matrix method for two multilayer structures with different top hBN layer thicknesses of 10 and 90 nm, respectively. Here, the electric field amplitude is normalized to that of the incident pump light, which is a plane wave normally incident on the multilayer structure. While keeping the thicknesses of the bottom hBN fixed to 330 nm, the thicknesses of SU8 layers are 195 and 282 nm, which enable the incident light to form standing waves. The standing waves inside the GTM behave in a way analogous to that in a one-side open pipe. Initially with a thin top hBN layer, the WSe_2 monolayer is located at the open side with the antinode of the standing wave, and as increasing the thickness of the top hBN layer, it moves to the nodal position. Additionally, adjusting the top-hBN layer's thickness can thus change the pump intensity and the Purcell factors of exciton complexes.

To further investigate the performance of the GTMs with different top hBN layers, we analyzed the electric field intensity of the pump light and the Purcell factor of the bright neutral exciton on the plane of the WSe_2 monolayer as a function of the SU8 layer thickness (Figure 4c). The GTM with a 10 nm thick top hBN layer can modulate the electric field interference at both pump and emission wavelengths of the bright neutral excitons, approaching the theoretical limit (the dotted lines in Figure 4c). In contrast, the GTM with a 90 nm thick top hBN layer exhibits a smaller modulation magnitude (see Supporting Information, Section S6 for more details). However, it creates narrow valleys of strong emission suppression (as shown by blue arrows in the right panel of Figure 4c), suitable for the generation of long-lived excitons, along with regions of fairly uniform vacuum fields between the valleys. Moreover, the suppressed radiative recombination indicated by the Purcell factor of less than unity allows the exciton complexes to have a longer lifetime.[34−38,43] Figure 4d presents comprehensive information on the electric field intensity at the pump wavelength and the Purcell factor at the emission wavelengths of the exciton complexes. The figure shows obvious periodic behavior as a function of the SU8 and top hBN layer thicknesses. Since the periodicities are different depending on the wavelength, a thicker top hBN layer can engineer the Purcell factors of each exciton complexes differently (Supporting Information, Section S7).

We experimentally demonstrated postprocessing manipulation of the exciton complex palette (Figure 4e). The postprocessing included not only optical thickness reconfiguration but also physical spatial position reconfiguration. First, an additional 80 nm thick hBN flake was transferred onto the sample presented in Figure 3. While the periodic spacing of the

https://doi.org/10.1021/acsnano.3c11214
ACS Nano 2024, 18, 5647−5655

bright regions remains constant before and after the transfer of the additional hBN flake, their relative brightness varied. As predicted in Figure 4c, with a 10 nm thick hBN layer, the highly diverse pump and emission conditions resulted in significantly varying PL intensities for each of the bright regions. The relative PL intensities of the four bright regions on average were 1.00, 0.04, 0.75, and 0.17, respectively. However, the additional top hBN layer led to more uniformly bright regions with relative PL intensities of 0.90, 0.49, 1.00, and 0.94. Second, we also physically moved the hBN/WSe_2/hBN heterostructure, which resulted in a shift of bright and dark stripes of the total PL emission by ∼1.60 μm in the direction indicated by the white arrow in Figure 4e (Supporting Information, Section S8). Additionally, the pump power dependence of the PL intensity of the exciton complexes would provide another degree of freedom for the exciton complex palette (Supporting Information, Section S9).

CONCLUSION

In this study, we demonstrated a 2D exciton complex palette utilizing spatial engineering of the optical vacuum field interference. The GTM effectively controlled the radiative decay dynamics and PL intensities of the exciton complexes separately, depending on their emission wavelengths. We successfully created and arranged five distinct compositions of the exciton complexes in the single WSe_2 monolayer. This purely optical technique allows for the observation and examination of minor exciton complexes, even at relatively high temperatures. The theoretical analysis of the pump intensity and Purcell factor in the GTM platform reproduced the experimental results. Moreover, the performance of the exciton complex palette can be tailored through postprocessing, either by introducing an additional optical layer or by physically shifting the hBN/WSe_2/hBN heterostructure. We expect that the exciton complex palette will be an efficient tool to investigate the dynamic properties and interactions of the exciton complexes and explore their potential for innovative excitonic devices.[17,20,26,44−46]

METHODS

Numerical Calculation and Theoretical Analysis. We employed the transfer matrix method in the numerical simulator (Lumerical, Ansys Canada Ltd.) to calculate the electric field intensity of the incident pump light. The refractive index of SU8 was fixed as 1.6. The Drude−Lorentz model was used for the refractive index of Al[47] and the refractive index of hBN.[48] The Purcell factor was calculated by the coherent optical feedback model considering the multiple reflections in the multilayer system (see Supporting Information, Section S3 for more details).

Sample Fabrication and Characterization. To fabricate the GTM platform, we first deposited an 80 nm thick Al layer on the Si substrate by radio frequency sputtering. Second, a layer of SU8 (SU8 2000.5) was spin-coated, followed by treatment with an UV lamp emitting light of 260 nm wavelength for 30 min and thermal annealing with a hot plate at 180 °C for 15 min. Using adhesive tape, the multilayer hBN flakes (National Institute for Materials Science (NIMS), Japan) and the monolayer WSe_2 flakes (2D Semiconductors Inc.) were physically exfoliated from the bulk crystals. Dry-transfer of the hBN/WSe_2/hBN heterostructure was performed by using the polyester stamp. Focused ion beam milling and scanning electron microscopy were used to measure the thicknesses of the SU8 layer and the top and bottom hBN layers (see Supporting Information, Section S2 for more details).

Measurement Setup. We employed a confocal microscopy setup combined with a cryogenic chamber (CS204-DMX-20-OM, Advanced Research Systems, Inc.) for PL spectral distribution measurements. A two-axis galvanometer mirror system (GVS102, Thorlabs, Inc.) was used to scan the area of interest. A 633 nm wavelength HeNe laser with a spot diameter of 1.33 μm was employed to excite the PL emission and was blocked by a 700 nm long-pass filter (FELH0700. Thorlabs, Inc.). A 20× long working-distance objective lens (NA = 0.40, Mitutoyo) collected the PL emission from the WSe_2 monolayer to the spectrometer system comprising a Czerny-Turner monochromator and a 2D array detector (SP2500 and PIXIS 100, Princeton Instruments).

ASSOCIATED CONTENT

Supporting Information

The Supporting Information is available free of charge at https://pubs.acs.org/doi/10.1021/acsnano.3c11214.

Exclusion of the effects of surface plasmon polaritons at the surface of the Al mirror; Measurement of the thickness of the SU8 layer and its gradient; Coherent optical feedback model analysis; Theoretical estimation of the PL intensity; PL spectra without normalization; Coherent feedback model analysis of postprocessing manipulation of the total PL intensity; Distinct engineering of Purcell factors for each exciton complexes depending on the top hBN layer thickness; Positional reconfiguration of the van der Waals heterostructure on the gradient thickness mirror; Pump power dependence of PL emission intensities of exciton complexes (PDF)

AUTHOR INFORMATION

Corresponding Author

Min-Kyo Seo − *Department of Physics, KAIST, Daejeon 34141, Republic of Korea;* orcid.org/0000-0003-0618-3955; Email: minkyo_seo@kaist.ac.kr

Authors

Sanghyeok Park − *Department of Physics, KAIST, Daejeon 34141, Republic of Korea*

Jaeyu Kim − *Department of Physics, KAIST, Daejeon 34141, Republic of Korea*

Dongha Kim − *Department of Physics, KAIST, Daejeon 34141, Republic of Korea;* Present Address: Department of Electrical Engineering, Ginzton Laboratory, Stanford University, Stanford, California 94305, U.S.A

Kenji Watanabe − *Research Center for Electronic and Optical Materials, National Institute for Materials Science, Tsukuba 305-0044, Japan;* orcid.org/0000-0003-3701-8119

Takashi Taniguchi − *Research Center for Materials Nanoarchitectonics, National Institute for Materials Science, Tsukuba 305-0044, Japan;* orcid.org/0000-0002-1467-3105

Complete contact information is available at: https://pubs.acs.org/10.1021/acsnano.3c11214

Author Contributions

‖S.P. and J.K. contributed equally to this work. S.P., J.K., and M.-K.S. conceived the project. S.P., J.K., and D.K. fabricated the gradient thickness mirrors. S.P., J.K., and D.K. fabricated the 2D heterostructures. S.P. and J.K. performed the confocal PL measurements. S.P. performed the theoretical calculations. K.W. and T.T. provided the boron nitride crystals. S.P., J.K., and M.-K.S. analyzed the data and wrote the manuscript with the assistance of all other authors.

Funding

M.-K.S. acknowledges support from the KAIST Cross-Generation Collaborative Lab Project and the National Research Foundation of Korea (NRF; 2020R1A2C2014685). S.P. acknowledges support from the National Research Foundation of Korea (NRF; RS-2023-00273230). D.K. acknowledges support from National Research Foundation of Korea (NRF; 2019R1A6A1A10073887). K.W. and T.T. acknowledge support from the JSPS KAKENHI (Grant Nos. 21H05233 and 23H02052) and World Premier International Research Center Initiative (WPI), MEXT, Japan.

Notes

The authors declare no competing financial interest.

REFERENCES

(1) Pei, J.; Yang, J.; Yildirim, T.; Zhang, H.; Lu, Y. Many-Body Complexes in 2D Semiconductors. *Adv. Mater.* **2019**, *31*, 1706945.
(2) Li, Z.; Wang, T.; Miao, S.; Lian, Z.; Shi, S. Fine structures of valley-polarized excitonic states in monolayer transitional metal dichalcogenides. *Nanophotonics.* **2020**, *9*, 1811−1829.
(3) Amani, M.; Lien, D.-H.; Kiriya, D.; Xiao, J.; Azcatl, A.; Noh, J.; Madhvapathy, S. R.; Addou, R.; KC, S.; Dubey, M.; Cho, K.; Wallace, R. M.; Lee, S.-C.; He, J.-H.; Ager, J. W.; Zhang, X.; Yablonovitch, E.; Javey, A. Near-unity photoluminescence quantum yield in MoS_2. *Science* **2015**, *350*, 1065−1068.
(4) Ye, Y.; Wong, Z. J.; Lu, X.; Ni, X.; Zhu, H.; Chen, X.; Wang, Y.; Zhang, X. Monolayer excitonic laser. *Nat. Photonics* **2015**, *9*, 733−737.
(5) Sun, Z.; Gu, J.; Ghazaryan, A.; Shotan, Z.; Considine, C. R.; Dollar, M.; Chakraborty, B.; Liu, X.; Ghaemi, P.; Kéna-Cohen, S.; Menon, V. M. Optical control of room-temperature valley polaritons. *Nat. Photonics* **2017**, *11*, 491−496.
(6) Dufferwiel, S.; Lyons, T. P.; Solnyshkov, D. D.; Trichet, A. A. P.; Withers, F.; Schwarz, S.; Malpuech, G.; Smith, J. M.; Novoselov, K. S.; Skolnick, M. S.; Krizhanovskii, D. N.; Tartakovskii, A. I. Valley-addressable polaritons in atomically thin semiconductors. *Nat. Photonics* **2017**, *11*, 497−501.
(7) Chen, Y.-J.; Cain, J. D.; Stanev, T. K.; Dravid, V. P.; Stern, N. P. Valley-polarized exciton-polaritons in a monolayer semiconductor. *Nat. Photonics* **2017**, *11*, 431−435.
(8) Lien, D. H.; Amani, M.; Desai, S. B.; Ahn, G. H.; Han, K.; He, J.-H.; Ager, J. W.; Wu, M. C.; Javey, A. Large-area and bright pulsed electroluminescence in monolayer semiconductors. *Nat. Commun.* **2018**, *9*, 1229.
(9) You, Y.; Zhang, X. X.; Berkelbach, T. C.; Hybertsen, M. S.; Reichman, D. R.; Heinz, T. F. Observation of biexcitons in monolayer WSe_2. *Nat. Phys.* **2015**, *11*, 477−481.
(10) Chen, G.; Bonadeo, N. H.; Steel, D. G.; Gammon, D.; Katzer, D. S.; Park, D.; Sham, L. J. Optically Induced Entanglement of Excitons in a Single Quantum Dot. *Science* **2000**, *289*, 1906−1909.
(11) He, Y. M.; Iff, O.; Lundt, N.; Baumann, V.; Davanco, M.; Srinivasan, K.; Höfling, S.; Schneider, C. Cascaded emission of single photons from the biexciton in monolayered WSe_2. *Nat. Commun.* **2016**, *7*, 13409.
(12) Barbone, M.; Montblanch, A. RP.; Kara, D. M.; Palacios-Berraquero, C.; Cadore, A. R.; De Fazio, D.; Pingault, B.; Mostaani, E.; Li, H.; Chen, B.; Watanabe, K.; Taniguchi, T.; Tongay, S.; Wang, G.; Ferrari, A. C.; Atatüre, M. Charge-tuneable biexciton complexes in monolayer WSe_2. *Nat. Commun.* **2018**, *9*, 3721.
(13) Robert, C.; Amand, T.; Cadiz, F.; Lagarde, D.; Courtade, E.; Manca, M.; Taniguchi, T.; Watanabe, K.; Urbaszek, B.; Marie, X. Fine structure and lifetime of dark excitons in transition metal dichalcogenide monolayer. *Phys. Rev. B* **2017**, *96*, 155423.
(14) Park, K. D.; Jiang, T.; Clark, G.; Xu, X.; Raschke, M. B. Radiative control of dark excitons at room temperature by nano-optical antenna-tip Purcell effect. *Nat. Nanotechnol.* **2018**, *13*, 59−64.
(15) Combescot, M.; Betbeder-Matibet, O.; Combescot, R. Bose−Einstein Condensation in Semiconductors: The Key Role of Dark Excitons. *Phys. Rev. Lett.* **2007**, *99*, 176403.
(16) Rosati, R.; Schmidt, R.; Brem, S.; Perea-Causín, R.; Niehues, I.; Kern, J.; Preuß, J. A.; Schneider, R.; Michaelis de Vasconcellos, S.; Bratschitsch, R.; Malic, E. Dark exciton anti-funneling in atomically thin semiconductors. *Nat. Commun.* **2021**, *12*, 7221.
(17) Chand, S. B.; Woods, J. M.; Quan, J.; Mejia, E.; Taniguchi, T.; Watanabe, K.; Alù, A.; Grosso, G. Interaction-driven transport of dark excitons in 2D semiconductors with phonon-mediated optical readout. *Nat. Commun.* **2023**, *14*, 3712.
(18) Wang, K.; De Greve, K.; Jauregui, L. A.; Sushko, A.; High, A.; Zhou, Y.; Scuri, G.; Taniguchi, T.; Watanabe, K.; Lukin, M. D.; Park, H.; Kim, P. Electrical control of charged carriers and excitons in atomically thin materials. *Nat. Nanotechnol.* **2018**, *13*, 128−132.
(19) Moody, G.; Tran, K.; Lu, X.; Autry, T.; Fraser, J. M.; Mirin, R. R.; Yang, L.; Li, X.; Silverman, K. L. Microsecond Valley Lifetime of Defect-Bound Excitons in Monolayer WSe_2. *Phys. Rev. Lett.* **2018**, *121*, 057403.
(20) Liu, H.; Wang, C.; Liu, D.; Luo, J. Neutral and defect-induced exciton annihilation in defective monolayer WS_2. *Nanoscale* **2019**, *11*, 7913.
(21) Yong, C. K.; Horng, J.; Shen, Y.; Cai, H.; Wang, A.; Yang, C.-S.; Lin, C.-K.; Zhao, S.; Watanabe, K.; Taniguchi, T.; Tongay, S.; Wang, F. Biexcitonic optical Stark effects in monolayer molybdenum diselenide. *Nat. Phys.* **2018**, *14*, 1092−1096.
(22) Hao, K.; Specht, J.; Nagler, P.; Xu, L.; Tran, K.; Singh, A.; Dass, C. K.; Schüller, C.; Korn, T.; Richter, M.; Knorr, A.; Li, X.; Moody, G. Neutral and charged inter-valley biexciton in monolayer $MoSe_2$. *Nat. Commun.* **2017**, *8*, 15552.
(23) Steinhoff, A.; Florian, M.; Singh, A.; Tran, K.; Kolarczik, M.; Helmrich, S.; Achtstein, A. W.; Woggon, U.; Owschimikow, N.; Jahnke, F.; Li, X. Biexciton fine structure in monolayer transition metal dichalcogenides. *Nat. Phys.* **2018**, *14*, 1199−1204.
(24) Chow, C. M.; Yu, H.; Jones, A. M.; Yan, J.; Mandrus, D. G.; Taniguchi, T.; Watanabe, K.; Yao, W.; Xu, X. Unusual Exciton-Phonon Interactions at van der Waals Engineered Interfaces. *Nano Lett.* **2017**, *17*, 1194−1199.
(25) Li, Z.; Wang, T.; Jin, C.; Lu, Z.; Lian, Z.; Meng, Y.; Blei, M.; Gao, M.; Taniguchi, T.; Watanabe, K.; Ren, T.; Cao, T.; Tongay, S.; Smirnov, D.; Zhang, L.; Shi, S. Momentum-Dark Intervalley Exciton in Monolayer Tungsten Disdelenide Brightened via Chiral Phonon. *ACS Nano* **2019**, *13*, 14107−14113.
(26) Jadczak, J.; Glazov, M.; Kutrowska-Girzycka, J.; Schindler, J. J.; Debus, J.; Ho, C.-H.; Watanabe, K.; Taniguchi, T.; Bayer, M.; Bryja, L. Upconversion of Light into Bright Intravalley Excitons via Dark Intervalley Excitons in hBN-Encapsulated WSe_2 Monolayers. *ACS Nano* **2021**, *15*, 19165−19174.
(27) Tang, H.; Luo, F.; Cui, Z.; Xiao, Y.; Xu, W.; Zhu, Z.; Chen, S.; Wang, X.; Liu, Y.; Wang, J.; Peng, G.; Qin, S.; Zhu, M. Electrically Controlled Wavelength-Tunable Photoluminescence from van der Waals Heterostructure. *ACS Appl. Mater. Interfaces* **2022**, *14*, 19869−19877.
(28) Chernikov, A.; van der Zande, A. M.; Hill, H. M.; Rigosi, A. F.; Velauthapillai, A.; Hone, J.; Heinz, T. F. Electrical Tuning of Exciton Binding Energies in Monolayer WS_2. *Phys. Rev. Lett.* **2015**, *115*, 126802.
(29) Harats, M. G.; Kirchhof, J. N.; Qiao, M.; Greben, K.; Bolotin, K. I. Dynamics and efficient conversion of excitons to trions in non-uniformly strained monolayer WS_2. *Nat. Photonics* **2020**, *14*, 324−329.
(30) He, K.; Poole, C.; Mak, K. F.; Shan, J. Experimental Demonstration of Continuous Electronic Structure Tuning via Strain in Atomically Thin MoS_2. *Nano Lett.* **2013**, *13*, 2931−2936.
(31) Conley, H. J.; Wang, B.; Ziegler, J. I.; Haglund, R. F., Jr; Pantelides, S. T.; Bolotin, K. I. Bandgap Engineering of Strained Monolayer and Bilayer MoS_2. *Nano Lett.* **2013**, *13*, 3626−3630.
(32) Li, Z.; Liu, C.; Rong, X.; Luo, Y.; Cheng, H.; Zheng, L.; Lin, F.; Shen, B.; Gong, Y.; Zhang, S.; Fang, Z. Tailoring MoS_2 Valley-

https://doi.org/10.1021/acsnano.3c11214
ACS Nano 2024, 18, 5647−5655

Polarized Photoluminescence with Super Chiral Near-Field. *Adv. Mater.* **2018**, *30*, 1801908.
(33) Luo, Y.; Shepard, G. D.; Ardelean, J. V.; Rhodes, D. A.; Kim, B.; Barmak, K.; Hone, J. C.; Strauf, S. Deterministic coupling of site-controlled quantum emitters in monolayer WSe_2 to plasmonic nanocavities. *Nat. Nanotechnol.* **2018**, *13*, 1137−1142.
(34) Fang, H. H.; Han, B.; Robert, C.; Semina, M. A.; Lagarde, D.; Courtade, E.; Taniguchi, T.; Watanabe, K.; Amand, T.; Urbaszek, B.; Glazov, M. M.; Marie, X. Control of the Exciton Radiative Lifetime in van der Waals Heterostructures. *Phys. Rev. Lett.* **2019**, *123*, 067401.
(35) Horng, J.; Chou, Y.-H.; Chang, T.-C.; Hsu, C.-Y.; Lu, T.-C.; Deng, H. Engineering radiative coupling of excitons in 2D semiconductors. *Optica.* **2019**, *6*, 1443−1448.
(36) Zhou, Y.; Scuri, G.; Sung, J.; Gelly, R. J.; Wild, D. S.; De Greve, K.; Joe, A. Y.; Taniguchi, T.; Watanabe, K.; Kim, P.; Lukin, M. D.; Park, H. Controlling Excitons in an Atomically Thin Membrane with a Mirror. *Phys. Rev. Lett.* **2020**, *124*, 027401.
(37) Rogers, C.; Gray, D.; Bogdanowicz, N.; Taniguchi, T.; Watanabe, K.; Mabuchi, H. Coherent feedback control of two-dimensional excitons. *Phys. Rev. Research.* **2020**, *2*, 012029.
(38) Park, S.; Kim, D.; Choi, Y.-S.; Baucour, A.; Kim, D.; Yoon, S.; Watanabe, K.; Taniguchi, T.; Shin, J.; Kim, J.; Seo, M.-K. Customizing Radiative Decay Dynamics of Two-Dimensional Excitons via Position- and Polarization-Dependent Vacuum-Field Interference. *Nano Lett.* **2023**, *23*, 2158−2165.
(39) Onga, M.; Zhang, Y.; Ideue, T.; Iwasa, Y. Exciton Hall effect in monolayer MoS_2. *Nat. Mater.* **2017**, *16*, 1193.
(40) Cadiz, F.; Robert, C.; Courtade, E.; Manca, M.; Martinelli, L.; Taniguchi, T.; Watanabe, K.; Amand, T.; Rowe, A. C. H.; Paget, D.; Urbaszek, B.; Marie, X. Exciton diffusion in WSe_2 monolayers embedded in a van der Waals heterostructure. *Appl. Phys. Lett.* **2018**, *112*, 152106.
(41) Datta, K.; Lyu, Z.; Li, Z.; Taniguchi, T.; Watanabe, K.; Deotare, P. B. Spatiotemporally controlled room-temperature exciton transport under dynamic strain. *Nat. Photonics* **2022**, *16*, 242−247.
(42) Huang, J.; Hoang, T.; Mikkelsen, M. Probing the origin of excitonic states in monolayer WSe_2. *Sci. Rep.* **2016**, *6*, 22414.
(43) Park, S.; Kim, D.; Seo, M.-K. Plasmonic Photonic Crystal Mirror for Long-Lived Interlayer Exciton Generation. *ACS Photonics* **2021**, *8* (12), 3619−3626.
(44) del Águila, A. G.; Wong, Y. R.; Wadgaonkar, I.; Fieramosca, A.; Liu, X.; Vaklinova, K.; Dal Forno, S.; Do, T. T. H.; Wei, H. Y.; Watanabe, K.; Taniguchi, T.; Novoselov, K. S.; Koperski, M.; Battiato, M.; Xiong, Q. Ultrafast exciton fluid flow in an atomically thin MoS_2 semiconductor. *Nat. Nanotechnol.* **2023**, *18*, 1012−1019.
(45) Chen, X.; Lu, X.; Dubey, S.; Yao, Q.; Liu, S.; Wang, X.; Xiong, Q.; Zhang, L.; Srivastava, A. Entanglement of single-photons and chiral phonons in atomically thin WSe_2. *Nat. Phys.* **2019**, *15*, 221−227.
(46) Jiang, C.; Xu, W.; Rasmita, A.; Huang, Z.; Li, K.; Xiong, Q.; Gao, W. Microsecond dark-exciton valley polarization memory in two-dimensional heterostructures. *Nat. Commun.* **2018**, *9*, 753.
(47) Rumble, J. *Handbook of Chemistry and Physics*; CRC, 2019; Chapter 12, pp 133−156.
(48) Lee, S.-Y.; Jeong, T.-Y.; Jung, S.; Yee, K.-J. Refractive Index Dispersion of Hexagonal Boron Nitride in the Visible and Near-Infrared. *Phys. Status Solidi B* **2019**, *256*, 1800417.

https://doi.org/10.1021/acsnano.3c11214
ACS Nano 2024, 18, 5647−5655